Electrostatic extension of magnetic proximity effect in $La_{0.7}Sr_{0.3}MnO_3$

Qianqian Lan[1*], Michael Schnedler[1], Lars Freter[1], Chuanshou Wang[2], Kurt Fischer[3], Philipp Ebert[1], and Rafal E. Dunin-Borkowski[1]

[1] Ernst Ruska-Centre for Microscopy and Spectroscopy with Electrons (ER-C-1) and Peter Grünberg Institut (PGI-5), Forschungszentrum Jülich GmbH, 52425 Jülich, Germany

[2] Department of Physics, Southern University of Science and Technology, Shenzhen 518055, People's Republic of China

[3] Department of Mechanical and Electrical Engineering, National Institute of Technology, Tokuyama College, Gakuendai, Shunan, Yamaguchi, 745-8585, Japan

Abstract

Magnetic proximity effects are typically limited to a few nanometers due to the short-range nature of the underlying magnetic interactions. Here, we use off-axis electron holography to reveal an electrostatically-induced long-range magnetic proximity effect that extends over a distance of 40 nm at a ferromagnetic/paramagnetic interface in $La_{0.7}Sr_{0.3}MnO_3$. We show that this behavior results from carrier diffusion and drift across the interface, which changes the Mn^{3+}/Mn^{4+} ratio and hence the local Curie temperature and density of magnetic moments.

Many fascinating magnetic effects emerge at interfaces between layers with different magnetic orders [1-5]. Interface confinement is intimately related to the magnetic proximity effect, which typically has a spatial extent of only a few atomic layers [3,6-9]. This short extent is due to the underlying physical coupling mechanisms, such as the exchange interaction, the Dzyaloshinsky-Moriya interaction [10], interface states [11-13], rehybridization [14,15], and reconstruction [16], all of which are highly localized. Here, we report an exceptionally long-range magnetic proximity effect reaching ~40 nm at a ferromagnetic (FM)/ paramagnetic (PM) interface in $La_{0.7}Sr_{0.3}MnO_3$ (LSMO). This wide extent arises from carrier diffusion and drift across the interface, which changes the Mn^{3+}/Mn^{4+} ratio and thereby the density of magnetic moments and local Curie temperature. We determine the carrier concentration dependence of the Curie temperature and unravel the physical mechanism of the electrostatic extension of magnetic proximity effects, fundamentally reshaping our understanding of micromagnetism in perovskites.

The LSMO film studied here was grown on a 0.5 wt% Nb-doped $SrTiO_3$ (STO) (001) substrate using pulsed laser deposition, as described in the Supplemental Material. An interruption occurred during growth of the LSMO film, resulting in a decrease in Mn composition. This changes the Mn^{3+}/Mn^{4+} ion ratio, responsible for a decrease in Curie temperature (T_C) from approximately T_{C1}=339±$^1_2$ K to T_{C2}=279±3 K between the different sublayers in the film, as measured using Superconducting Quantum Interference Device (SQUID) magnetometry in a bath cryostat. (For details, see [17]). Between the two T_C values, the LSMO film therefore exhibits a *spatial* FM to PM transition. It should be noted that this system exhibits a strain-free, unreconstructed model interface within the same material [17]. Thus, lattice-strain-induced magnetostrictive effects [18] are absent and only T_C varies between adjacent sublayers as a result of doping. Based on classical micromagnetics, only the exchange interaction is relevant and the extent of the magnetic proximity effect can be expected to be in the 1 to 3 nm range, which is far below the value measured below.

Figures 1b and 1d show magnetic induction maps reconstructed from magnetic phase images recorded using off-axis electron holography (EH) at 295 and 280 K, respectively (see Supplemental Material), from the junction between the FM and PM LSMO layers. The density and direction of the phase contours reveal the strength and direction of the projected in-plane magnetic induction. Electron holographic tomography experiments show that no measurable out-of-plane magnetization component is present (see Fig. S2-S4 in the Supplemental Material).

The position of the FM/PM LSMO interface was determined by measuring the Mn concentration of the same region in the same lamella using energy-dispersive X-ray spectroscopy (EDX) (Fig. 1e). The results show that the Mn concentration decreases from the FM layer to the PM layer by 2.7±0.3% over a distance that has a full-width at half-maximum of 6.9±1.3 nm, as derived from a hyperbolic tangent fit (red line). The FM/PM interface is defined as the inflection point of the fit (marked by a dashed orange line).

In Figs 1b and 1d, the gray scale maps show electron optical phase contours that run parallel to the interface on the FM (left) side. The green arrows in Figs. 1a and 1c visualize the corresponding two-dimensional projected in-plane magnetization, derived using a model-based iterative reconstruction algorithm [19], revealing the direction and strength of magnetic moments oriented parallel to the interface. Deep on the PM (right) side only noise can be discerned, indicating no overall alignment of the magnetic moments, *i.e.*, a PM state. Close to the interface, the phase contour lines increasingly develop a preferential orientation parallel to the interface, indicating a penetration of FM order into the PM layer. This penetration depth increases at lower temperature from ~10 nm at 295 K to ~35 nm at 280 K.

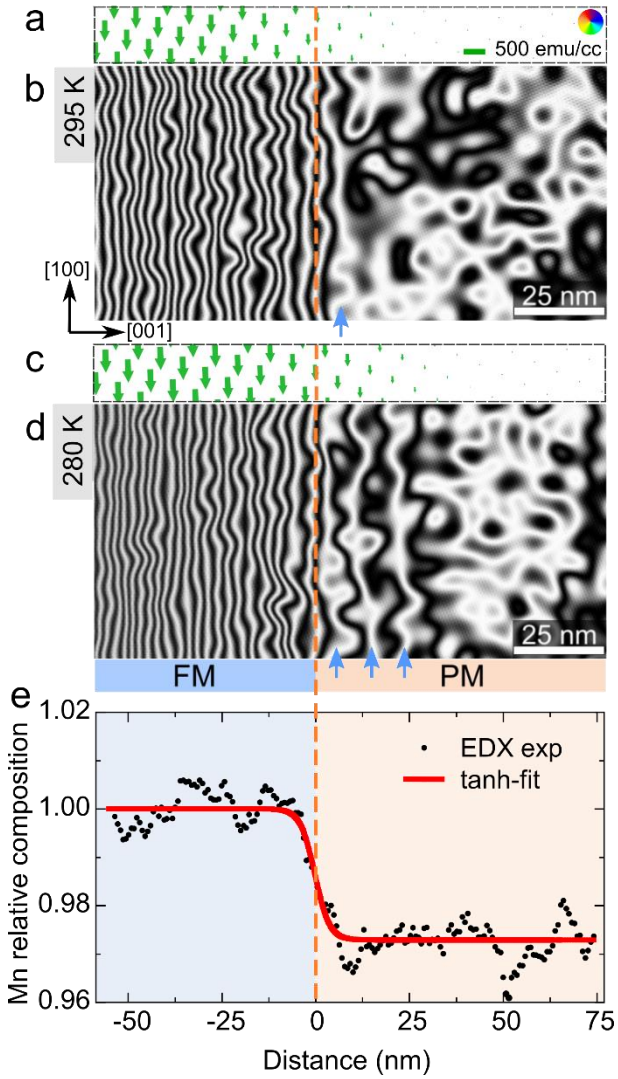

Figure 1. Magnetic induction maps of a FM/PM interface between two LSMO layers with slightly different Mn compositions determined from the magnetic contribution to the phase shift (b, d) measured using off-axis electron holography at 295 and 280 K, respectively. The contour spacing is π/25 radians. (a) and (c) show the corresponding magnitude and orientation of the projected in-plane magnetization determined from (b) and (d) using a model-based iterative reconstruction

algorithm. (e) Line profile of the Mn composition measured using EDX at the same location as (b) and (d). The inflection point of the hyperbolic tangent fit (red line) is defined as the spatial position of the interface between the FM and PM layers and is marked by a dashed orange line. The noise on the right side (appearing as a circular pattern) in the magnetic induction maps in (b) and (d) is indicative of a PM state, while the vertical lines on the left side result from alignment of the magnetization in the FM layer. The blue arrows mark phase contour lines with weaker alignment of the magnetization penetrating into the PM layer.

In order to obtain quantitative insight into the penetration of FM order into the PM layer at the FM/PM interface, Fig. 2 shows the first derivative of the magnetic phase shift dφ/dx plotted as a function of position for different temperatures between and below the two T_C values. Since magnetic fringing fields are negligible according to a MuMax3 simulation (see below), the gradient of the phase shift dφ/dx measured using EH is proportional to the average projected in-plane magnetization multiplied by the experimentally determined magnetically active thickness of the lamella in the electron beam direction (see Supplemental Material), with a proportionality constant of $\frac{2\pi\mu_0 e}{h}$ [20]. The corresponding magnetization values are given on the right axis in Fig. 2. The results show that the magnetization in the FM layer is above 10^5 A/m at each investigated temperature. In the PM layer, no magnetization can be detected at 295 and 280 K far (*i.e.,* >40 nm) from the interface position at both temperatures above T_{C2}. Close to the interface, a region with non-zero magnetization is present on the PM layer side, with an extent that increases from 13.3±1.8 nm at 295 K to $38\pm^{8}_{4}$ nm at 280 K, revealing that FM order penetrates into the PM layer. At temperatures below T_{C2}, non-zero magnetization is present everywhere, as the PM layer becomes fully FM.

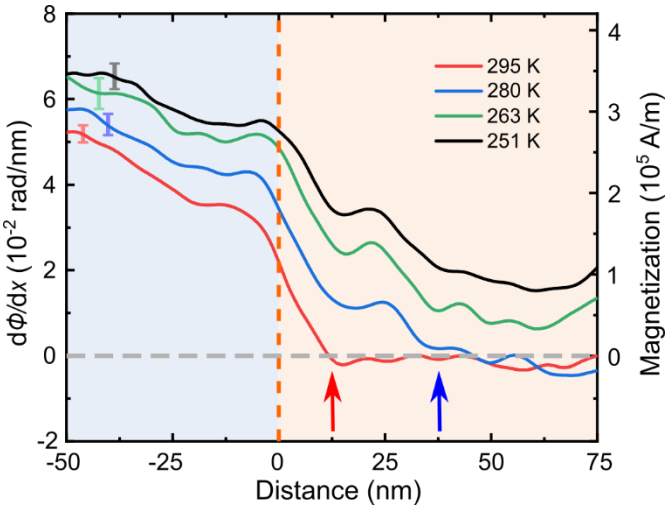

Figure 2. First derivative of the magnetic contribution to the phase shift dφ/dx (left axis) plotted as a function of distance from the PM/FM interface (x = 0 nm) along [001] in the LSMO film at 295 K (red), 280 K (blue), 263 K (green) and 251 K (black). The derivative of the magnetic

contribution to the phase shift dφ/dx measured using off-axis electron holography can be converted to units of average in-plane magnetization (right axis, see text for details). The slight slope is the FM layer is attributed partially to a small thickness change of the TEM lamella (see Fig. S1 in the Supplemental Material).

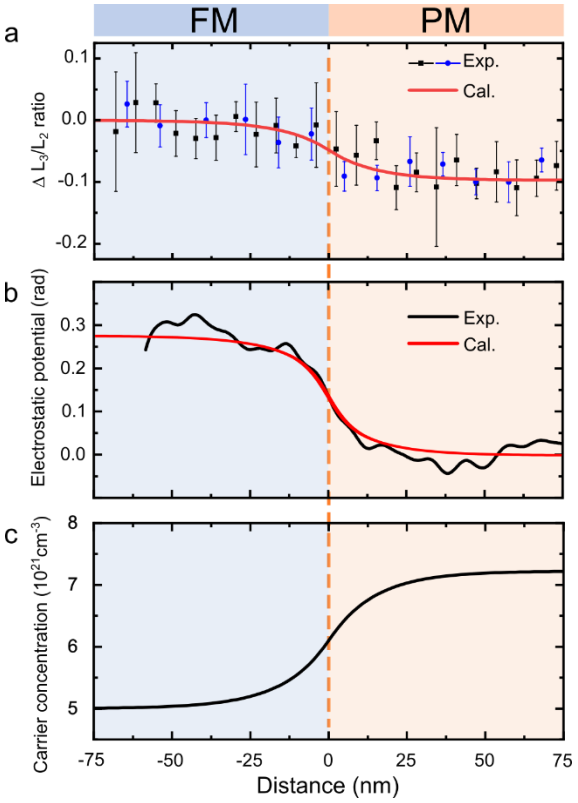

Figure 3. (a) Change in L_3/L_2 edge ratio measured using EELS at the same location as in Fig. 1 (black squares) and, for comparison, in a different lamella (blue dots). The red line shows the change in L_3/L_2 ratio calculated on the basis of carrier diffusion and drift visible in (c). (b) Electrostatic contribution to the phase shift (black) measured using off-axis electron holography at 295 K, compared to a simulation (red) based on the calculated electrostatic potential induced by carrier redistribution (see (c)) and to the change in mean inner potential associated with the change in Mn composition. (c) Carrier concentration plotted as a function of distance from the FM/PM interface.

Since the magnetic properties in this material are governed by the Mn^{3+}/Mn^{4+} double exchange interaction and hence can be influenced by the free carrier distribution [17], the local variation in electronic properties across the FM/PM interface needs to be considered. For this purpose, changes in the Mn L-edge across the sample were measured using EELS at 295 K. The resulting integrated L_3/L_2 edge ratio change is shown in Fig. 3a. A clear decrease is visible from

the FM to the PM layer by 0.097±0.015. This result indicates a corresponding Mn valence change, which can be quantified using the known linear dependence of the L_3/L_2 edge ratio on valence state, which has a slope of -0.73±0.11 [21]. Based on this relationship, we infer a change in Mn valence of ΔV = 0.133±0.029 between the FM and PM layer, with a smooth transition between the layers over a width of 57±16 nm at 295 K. This change in valence agrees well with that probed at 150 K below both T_{C1} and T_{C2}, [17], suggesting that it is determined primarily by the composition. This value of ΔV can be compared to a calculation based on the Mn composition change δ in $(La_{0.7}Sr_{0.3})^{2.7}Mn_{1-\delta}^{3.3+\Delta V}(O_3)^{-6}$ of 2.7±0.3% measured at the same location (Fig. 1c), on the assumption of charge neutrality and that the valence states and compositions of other elements (Sr, La and O) are unchanged. This approach yields a Mn valence change ΔV of 0.09±0.01, in close agreement with the value derived from the L_3/L_2 edge ratio.

The change in Mn valence can be expected to be related to the spatial redistribution of charge carriers. This relationship was assessed experimentally based on the electrostatic contribution to the electron optical phase shift measured using EH, which is sensitive to local variations in electrostatic potential and mean inner potential, *i.e.*, to charge carrier redistribution and chemical composition change, respectively. Figure 3b shows the electrostatic contribution to the phase shift across the layers (black line) measured at 295 K. The profile reveals an offset between the PM and FM layers across a transition region, whose extended width is consistent with that of the charge distribution in Fig. 3c discussed below. It is important to note that a sharp interface region with a width of only ~7 nm (see Fig. 1c) would be measured if solely the contribution from the mean inner potential were taken into account.

In order to assess the electrostatic properties of the layers, we note that the increase in average Mn valence of ΔV=+0.133 determined using EELS decreases the ideal stoichiometric 70% occupation of the Mn e_g state to 56.7% and thereby increases the free carrier (*i.e.*, hole) concentration in LSMO [17] from 5×10^{21} cm^{-3} in the FM layer to 7.22×10^{21} cm^{-3} in the PM layer, resulting in a step in carrier concentration at the interface. This composition-induced step in the carrier concentration is smoothed by carrier diffusion and drift, in analogy to a *p*-*n* junction. The diffusion is counterbalanced by the build-up of an electric field, thereby creating a depletion-zone-like region. This situation was modelled by self-consistently solving the Poisson and continuity equations within the framework of the drift and diffusion model [22,23] for a permittivity of 3×10^4 [24]. As shown in Fig. 3c, the drift and diffusion of free carriers at 295 K leads to a wide transition region with a FWHM of 35 nm between the two regions with different carrier concentrations.

Furthermore, the electrostatic phase profile was simulated by considering both the charge-carrier-induced electrostatic contribution to the electrostatic potential and the Mn-concentration-difference-induced change in mean inner potential. A mean inner potential change of 0.13 V was estimated for a Mn concentration change of 3% on the basis of a mean inner potential value of 18.7 V for LSMO [25] by using a simple *Z*-dependent approximation for the electron scattering factors. The simulated electrostatic potential profile matches the experimental electrostatic phase shift measured using off-axis EH well, as shown in Fig. 3b.

Similarly, the calculated charge carrier profile was used to determine the valence change profile and the expected $\Delta L_3/L_2$ edge ratio (Fig. 3a, red line). The simulated and experimental values agree well.

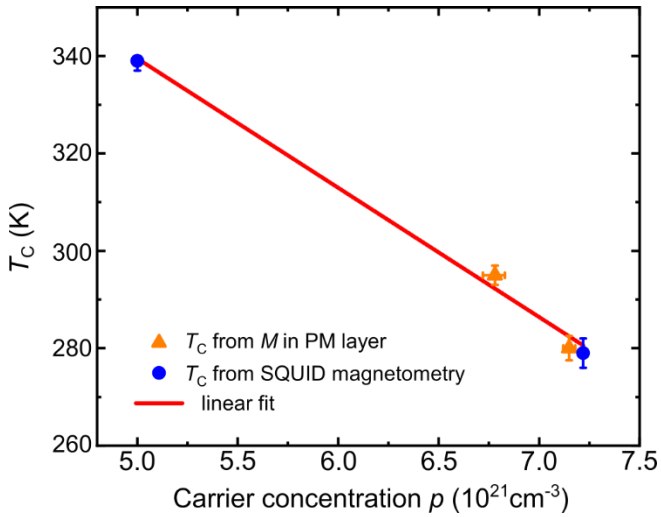

Figure 4. Curie temperature (T_C) determined using SQUID magnetometry (blue dots) and off-axis electron holography (orange triangles), plotted as a function of carrier concentration. The red fitting line is consistent with a linear relationship between T_C and carrier concentration.

Both the extent of the electrostatic transition region and the penetration of FM order into the PM layer are much wider than expected for a typical magnetic proximity effect based on the exchange interaction between neighboring magnetic atoms. Because the exchange interaction is fundamentally linked to the overlap of electron wave functions and electron-electron Coulomb interactions, it is intrinsically short-range. Indeed, a MuMax3 simulation [26] considering only magnetic interactions yields an interface width smaller than 1 nm and that stray fields are negligible. Thus, in the present case, other effects, notably the free carriers, play a dominant role.

For a deeper understanding of the influence of the free carrier density, we recall that in LSMO free holes are hopping between Mn ions along Mn^{3+}-O^{2-}-Mn^{4+}chains in the Mn e_g states. Thereby the valence of the Mn ions varies locally and temporally, although its average value is unchanged. At the interface between PM and FM LSMO layers with different free carrier concentrations, drift and diffusion of holes create a steady state carrier redistribution profile, which modifies the spatial distribution of the average Mn valence and hence the Mn^{3+}/Mn^{4+} ion ratio. Since FM ordering originates from the Mn^{3+}-Mn^{4+} double exchange interaction, this change in Mn valence directly affects the density of magnetic moments, *i.e.*, the magnetization. Simultaneously, the change in Mn^{3+}/Mn^{4+} ion ratio affects the local value of T_C.

Therefore, we determine the dependence of T_C on the free carrier concentration as follows: First, at measurement temperatures of 295 and 280 K we find that the magnetization reaches zero at distances of 13.3±1.8 and $38\pm^{8}_{4}$ nm from the chemical FM/PM interface inside the PM layer (see Fig. 2, red and blue arrows), respectively. At these distances, the measurement temperature corresponds to the local value of T_C. The corresponding values of carrier concentration can be determined from the calculation in Fig. 3c. The resulting values of T_C *vs* free hole concentration are shown in Fig. 4. In addition, for the values of $T_{C1}=339\pm^{1}_{2}$ K and T_{C2}=279±3 K of the two LSMO layers far from the interface, as determined from the SQUID measurement, the corresponding asymptotic hole concentration is given in Fig. 3c and included in Fig. 4. Figure 4 reveals a linear dependence of T_C on hole concentration, which can be understood in terms of a change of valence with hole concentration and thus the change in Mn^{3+}/Mn^{4+} ion ratio, which directly affects the double exchange interaction between the Mn^{3+} and Mn^{4+} ions. The importance of the determined dependence of T_C on hole concentration lies in the fact that T_C is usually affected by both strain and carrier concentration, making it impossible to obtain a clear-cut physical understanding. In the here investigated system, no strain is present and thus the carrier dependence of T_C becomes accessible. Therefore, the exceptionally long-range magnetic proximity effect that we observe is induced by the large spatial extent of the diffusion and drift of the free holes, which in turn arises from a combination of a high dielectric constant and a low free carrier concentration when compared to a metal.

The effect that we observe here can be expected to occur widely, for example in perovskites or two-dimensional ferromagnetic materials in which the valence of the magnetic ions can be altered by a change in composition as well as by tuning the carrier distribution through doping or application of electric fields. Our results unravel a microscopic mechanism and provide a quantitative relationship between electrostatic properties (*i.e.*, local hole concentration and Mn valence) and local magnetization, as well as Curie temperature. This quantitative relationship defines the spatial extent of the electrostatically-extended magnetic proximity effect and provides a fundamental understanding of the electrostatic-shaping of nanoscale magnetism.

Acknowledgments

This project has received funding from the European Research Council (ERC) under the European Union's Horizon 2020 research and innovation programme (Grant No. 856538, project "3D MAGiC"). The authors thank M. Kruth, L. Kibkalo and L. Risters for specimen preparation using focused ion beam milling as well as K. Ji, L. Jin, A. Kovács, F. Zheng, and X. Zhong for valuable discussions.

References

[1] F. Hellman, A. Hoffmann, Y. Tserkovnyak, G. S. D. Beach, E. E. Fullerton, C. Leighton, A. H. MacDonald, D. C. Ralph, D. A. Arena, H. A. Dürr et al., Rev. Mod. Phys. 89, 025006 (2017).

[2] L. J. Riddiford, A. J. Grutter, T. Pillsbury, M. Stanley, D. Reifsnyder Hickey, P. Li, N. Alem, N. Samarth, and Y. Suzuki, Phys. Rev. Lett. **128**, 126802 (2022).
[3] D. Zhong, K. L. Seyler, X. Linpeng, N. P. Wilson, T. Taniguchi, K. Watanabe, M. A. McGuire, K. C. Fu, D. Xiao, W. Yao, and X. Xu, Nat. Nanotechnol. **15**, 187 (2020).
[4] I. Žutić, A. Matos-Abiague, B. Scharf, H. Dery, and K. Belashchenko, Mater.Today **22**, 85 (2019).
[5] P. Wei, S. Lee, F. Lemaitre, L. Pinel, D. Cutaia, W. Cha, F. Katmis, Y. Zhu, D. Heiman, J. Hone, J. S. Moodera, and C. T. Chen, Nat. Mater. **15**, 711 (2016).
[6] P. K. Manna and S. M. Yusuf, Phys. Rep. **535**, 61 (2014).
[7] C. Clavero, J. R. Skuza, Y. Choi, D. Haskel, C. Sánchez-Hanke, R. Loloee, M. Zhernenkov, M. R. Fitzsimmons, and R. A. Lukaszew, Phys. Rev. B **80**, 024418 (2009).
[8] J. S. Moodera, M. E. Taylor, and R. Meservey, Phys. Rev. B **40**, 11980 (1989).
[9] H. B. Vasili, M. Gamino, J. Gazquez, F. Sanchez, M. Valvidares, P. Gargiani, E. Pellegrin, and J. Fontcuberta, ACS Appl Mater Interfaces **10**, 12031 (2018).
[10] T. Moriya, Phys. Rev. **120**, 91 (1960).
[11] V. K. Lazarov, M. Weinert, S. A. Chambers, and M. Gajdardziska-Josifovska, Phys. Rev. B **72**, 195401 (2005).
[12] C. Kim and Y.-C. Chung, Appl. Phys. Lett. **88**, 132512 (2006).
[13] S. Eremeev, V. Men'Shov, V. Tugushev, P. M. Echenique, and E. V. Chulkov, Phys. Rev. B **88**, 144430 (2013).
[14] X. Qian and W. Hübner, Phys. Rev. B **67**, 184414 (2003).
[15] R. Tyer, G. van der Laan, W. M. Temmerman, Z. Szotek, and H. Ebert, Phys. Rev. B **67**, 104409 (2003).
[16] E.-M. Choi, K. I. Sim, K. S. Burch, and Y. H. Lee, Adv. Sci. 9, 2200186 (2022).
[17] See Supplemental Material at http://link.aps.org/supplemental/ 10.1103/PhysRevB.108.L180410 for sample preparation, temperature measurement, TEM characterization, and determination of out-of-plane magnetization by electron holographic tomography.
[18] Q. Lan, C. Wang, L. Jin, M. Schnedler, L. Freter, K. Fischer, J. Caron, X.-K. Wei, T. Denneulin, A. Kovács, P. Ebert, X. Zhong, and R. E. Dunin-Borkowski, Phys. Rev. Lett. **129**, 057201 (2022).
[19] M. W. Haverkort, S. I. Csiszar, Z. Hu, S. Altieri, A. Tanaka, H. H. Hsieh, H. J. Lin, C. T. Chen, T. Hibma, and L. H. Tjeng, Phys. Rev. B **69**, 020408(R) (2004).
[20] J. Caron, RWTH Aachen University, PhD Thesis (2017).
[21] T. Kasama, M. Beleggia, and R. E. Dunin-Borkowski, *Electron holography of magnetic materials* (intechopen London, United Kingdom, 2011), p.^pp. 57-61.
[22] M. Varela, M. P. Oxley, W. Luo, J. Tao, M. Watanabe, A. R. Lupini, S. T. Pantelides, and S. J. Pennycook, Phys. Rev. B **79**, 085117 (2009).
[23] M. Schnedler, R. Dunin-Borkowski, and P. Ebert, Phys. Rev. B **93**, 195444 (2016).
[24] M. Schnedler, V. Portz, P. Weidlich, R. Dunin-Borkowski, and P. Ebert, Phys. Rev. B **91**, 235305 (2015).
[25] S. Majumdar, H. Huhtinen, P. Paturi, and H. S. Majumdar, J. Mater. Sci. **48**, 2115 (2013).
[26] T. Kasama, M. S. Moreno, R. E. Dunin-Borkowski, S. B. Newcomb, N. Haberkorn, J. Guimpel, and P. A. Midgley, Appl. Surf. Sci. **252**, 3977 (2006).
[27] A. Vansteenkiste, J. Leliaert, M. Dvornik, M. Helsen, F. Garcia-Sanchez, and B. Van Waeyenberge, AIP Advances **4** (2014).

Supplemental Material
Electrostatic extension of magnetic proximity effect in $La_{0.7}Sr_{0.3}MnO_3$

Qianqian Lan[1*], Michael Schnedler[1], Lars Freter[1], Chuanshou Wang[2], Kurt Fischer[3], Philipp Ebert[1], and Rafal E. Dunin-Borkowski[1]

[1] Ernst Ruska-Centre for Microscopy and Spectroscopy with Electrons (ER-C 1) and Peter Grünberg Institute (PGI-5), Forschungszentrum Jülich GmbH, 52425 Jülich, Germany

[2] Department of Physics, Southern University of Science and Technology, Shenzhen 518055, People's Republic of China

[3] Department of Mechanical and Electrical Engineering, National Institute of Technology, Tokuyama College, Gakuendai, Shunan, Yamaguchi, 745-8585, Japan

Sample preparation.

The $La_{0.7}Sr_{0.3}MnO_3$ (LSMO) film was grown on a 0.5 wt% Nb-doped $SrTiO_3$ (STO) (001) substrate using pulsed laser deposition. The Mn composition change is associated with an interruption in growth. Specimens were prepared for transmission electron microscopy (TEM) by using focused ion beam milling in an FEI Helios Nanolab 400s dual-beam system. Surface damage was reduced by using Ar ion beam sputtering in a Fischione Nanomill 1040 system. The thickness of the lamella in the electron beam direction was measured to be approximately 120 nm using scanning electron microscopy and determined independently using a log-ratio technique based on electron energy-loss spectroscopy (EELS). In the analysis, the magnetically active thickness was taken to be 110±6 nm in the electron beam direction. It should be noted that the weak thickness change along the growth direction (Fig. S1) is small across the FM/PM transition region and hence does not significantly affect the large magnetization transition at the FM/PM interface investigated here.

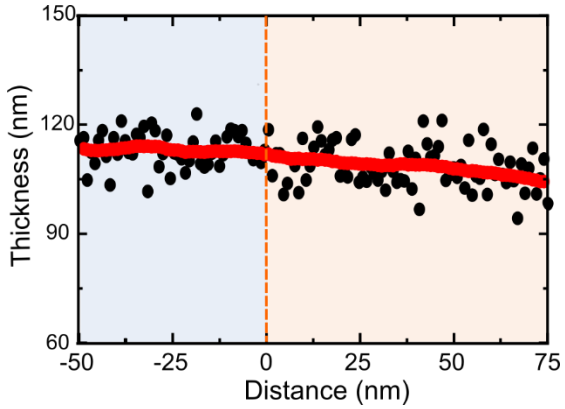

Fig. S1: Thickness measured across the FM/PM interface by EELS using the log-ratio technique vs. distance along growth direction. A slight decrease in thickness is found as a minor effect.

TEM characterization.

The chemical composition and Mn valence state were investigated in an FEI Titan G2 80-200 TEM with a four-quadrant Super-X EDX detector at 200 kV using energy-dispersive X-ray spectroscopy (EDX) and EELS [1]. For the EDX measurement, a probe convergence semi-angle of 24.7 mrad, a probe current of 28.3 pA and a detector collection solid angle of 0.7 sr were used. Maps were recorded at the [010] zone axis. The EDX results were recorded and analysed using Velox software, with a dwell time of 100 µs per pixel and with multiple fast frames accumulated until the sample drifted out of the maximum range for drift compensation. Binning of the experimental data and line profiles (integrating and averaging) was carried out to improve the total signal to noise ratio. Curve fitting by gaussians was then performed. For EELS, a Gatan Enfinium ER (model 977) electron energy-loss spectrometer with DUAL EELS was used. EEL spectra were recorded using a convergence semi-angle of 24.7 mrad and a collection semi-angle of 29 mrad at a dispersion of 0.25 eV per pixel. The energy resolution was 1.25 eV based on the full width at half maximum of the zero-loss peak. Multiple scattering was considered using Fourier-log deconvolution.

For magnetic imaging, off-axis electron holography (EH) was performed in an image-C_S-corrected FEI Titan 80-300 TEM at 300 kV [2]. A liquid-nitrogen-cooled double tilt specimen holder (Gatan model 636) was used to vary the specimen temperature. Off-axis electron holograms were recorded in magnetic-field-free conditions using a direct electron-counting camera (Gatan K2 IS). Maps of the electron optical phase shift φ were reconstructed from off-axis electron holograms digitally using HoloWorks software. The electron optical phase shift contains both electrostatic and magnetic contributions. In order to separate them, the lamella was tilted to 70 in opposite directions parallel to the ferromagnetic/paramagnetic interface and subjected to the magnetic field of the objective lens of the microscope. In each case, the sample was then tilted back to 0° in zero field and the electrostatic and magnetic components were extracted by calculating half of the sum and half of the difference, respectively, between aligned phase images reconstructed from pairs of holograms recorded with opposite magnetization directions in the sample.

The EDX, EELS, and EH results were recorded from the same region of the sample and aligned based on the positions of the LSMO/STO and LSMO/carbon interfaces.

Temperature measurement.

During transmission electron microscopy measurements, the temperature was probed by a Si diode located on the metal plate on which the TEM sample was clamped. Due to the location of the Si diode near the cooling Cu braid and the clamping contact of the sample, the true sample temperature is expected to be slightly higher than the measured value. We anticipate that a measured temperature of 278 K corresponds to a sample temperature close to 280 K. This difference is in line with the observation of a paramagnetic LSMO layer using off-axis electron holography at a nominal temperature of 278 K, despite the fact that T_{C2} was measured to be 279 K using Superconducting Quantum Interference Device measurements. The measured temperature of 278 K was therefore corrected and given as 280±2 K.

Electron holographic tomography.

In order to determine the out-of-plane component of magnetization in the sample, the TEM lamella was rotated with respect to the electron beam direction at 295 K, as shown schematically in Fig. S2. The rotation axis is the *z* axis. Thus, no overlap between the FM and PM layers occurs with rotation angle.

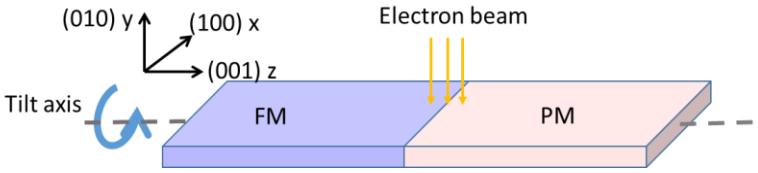

Fig. S2. Schematic diagram showing the tilt axis used for electron holographic tomography. The tilt axis is the *z* axis and the interface is parallel to the *xy* plane. Thus, the electron beam direction is parallel to the FM/PM interface at all sample tilt angles, with no overlap between the FM and PM layers.

Figure S3 shows a right-side view of the lamella in Fig. S2. The phase change induced by the magnetization is given by the expression

$$\frac{d\varphi}{dx} \sim M_{\text{in}} \cdot d_{\text{eff}} = M \cdot d \cdot cos(\beta) \cdot \big(1 - tan(\beta)tan(\alpha)\big), \qquad (1)$$

where α is the tilt angle of the lamella (during tomographic rotation) and β is the rotation angle of the magnetization away from the in-plane direction. d_{eff} is the effective thickness of the lamella in electron beam direction changing due to tilting. According to Eq. (1), for only in-plane magnetization (i.e. β=0) $\frac{d\varphi}{dx} \sim M \cdot d$ is constant and independent of the tilt angle α of the lamella.

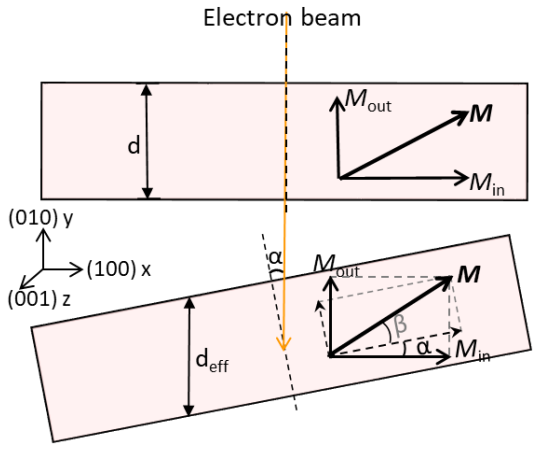

Fig. S3: Schematic cross-section, perpendicular to the rotation axis shown in Fig. S2. The figure illustrates the effect of tilt on the magnetization projected along the electron beam direction. Equation (1) describes the tilt dependence of the gradient of the electron optical phase shift.

Values of $\frac{\mathrm{d}\varphi}{dx}$ are plotted in Fig. S4 and are observed to be constant in the FM layer (black dots) and zero in PM layer for every measurement. Based on the error bars and on the absolute values of the measurements, no measurable out-of-plane component of the magnetization was detected. The orientation of the magnetization in the two sublayers is therefore inferred to be in-plane and parallel.

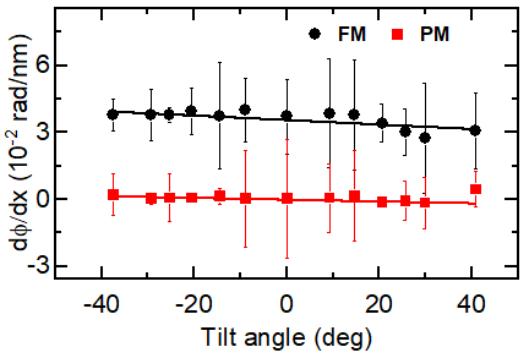

Fig. S4*: Results of electron holographic tomography, showing the gradient of the electron optical phase plotted as a function of tilt angle (with the tilt axis parallel to [001]) in the PM and FM layers at 295 K. The data show that the magnetization has no measurable out-of-plane component.*

1. Ernst Ruska-Centre for Microscopy and Spectroscopy with Electrons (ER-C) et al. (2016). FEI Titan G2 80-200 CREWLEY. Journal of large-scale research facilities. FEI Titan G2 80-200 CREWLEY. *Journal of large-scale research facilities JLSRF* **2,** (2016).

2. Ernst Ruska-Centre for Microscopy and Spectroscopy with Electrons (ER-C) et al. (2016). FEI Titan G2 60-300 HOLO. Journal of large-scale research facilities. FEI Titan G2 60-300 HOLO. *Journal of large-scale research facilities JLSRF* **2,** (2016).